KSCE Journal of Civil Engineering (2023) 27(8):3542-3554
DOI 10.1007/s12205-023-0106-0

pISSN 1226-7988, eISSN 1976-3808
www.springer.com/12205

Surveying and Geo-Spatial Engineering

Photogrammetric 3D Scanning of Asphalt Cores for Automatic Layer Detection and Gradation Classification

Joshua Carpenter[a], **Jinha Jung**[a], **and Jusang Lee**[b]

[a]Lyles School of Civil Engineering, Purdue University, West Lafayette, IN 47907, USA
[b]Office of Research and Development, Indiana Department of Transportation, West Lafayette, IN 47907, USA

ARTICLE HISTORY

Received 24 January 2023
Accepted 24 April 2023
Published Online 13 June 2023

KEYWORDS

Close-range photogrammetry
Asphalt core
Non-destructive analysis
3D scanning

ABSTRACT

Asphalt cores are routinely drilled from existing roadways and manually tested to determine the thickness of individual layers and classify the gradation of the aggregate mixture within each layer. This process is time-consuming, hazardous, and destroys the sample core. This study presents a non-destructive, close-range photogrammetry-based 3D scanning method for determining the layer divisions and aggregate gradation within asphalt cores. The proposed method uses structure-from-motion techniques to produce distortion-free images of the cylindrical surface of the core exposed during drilling. From these images, the asphalt mix gradation is determined from the exposed cross sections of aggregate within the core. Our method achieved a 75% classification accuracy and did not damage the sample, leaving the core intact for other uses. Additionally, we also find that surface image-based methods for gradation curve generation tend to underestimate the amount of smaller aggregate within a mix and show signs of higher variability in detecting the largest sizes of aggregate. This study demonstrates that the close-range photogrammetry-based 3D scanning technology can easily be developed into an automatic and non-destructive tool for asphalt core analysis.

1. Introduction

The pavement material commonly referred to as “asphalt” is a mixture of varying-sized aggregates and a bituminous binder, typically asphalt. To form a roadway from asphalt, workers spread the mixture flat with a paving machine and then compact it with rollers. Most roadways are built by laying and compacting successive layers of asphalt mixture. Within a finished roadway, the aggregate is the component that bears the weight of traffic; thus, the performance of each layer of asphalt is determined by the properties of the aggregate within each layer. Chief among these properties is the range of aggregate sizes found within the layer (Chen and Liew, 2002). This mix of aggregate sizes is called aggregate gradation.

Manual methods for determining the gradation of aggregate within an existing layer of asphalt pavement are used in departments of transportation across the United States. As an example, the Indiana Department of Transportation (INDOT) routinely examines drilled pavement samples (called cores) for both research and regulatory purposes. The cylindrical cores show a cross-section of the roadway layers. INDOT guidelines require that the layers of the core be cut apart and then treated with heat and solvents to break down the asphalt which binds the aggregate together. Once separated, the aggregate is put through a gradation testing machine that divides the aggregate by sieve size. The percentage of aggregate within each sieve size determines the gradation classification of the aggregate mixture (INDOT, 2021; INDOT, 2022). This manual process requires many hours for a technician to complete, is potentially hazardous, and destroys the core making it unusable in other tests (Buchanan and Brown, 1999). This paper discusses the viability of using photogrammetric techniques to detect the interfaces between layers and the aggregate gradation within each layer through a non-destructive process.

One of the first attempts to use digital imagery to analyze the aggregate within an asphalt core was completed in 1995 by Yue et al. (1995). The core to be analyzed was cut in cross-sections to create thin circular disks. These disks were scanned on a flatbed scanner and digital image processing techniques detected the distribution, orientation, and shape of coarse aggregate within the cross-section. This work, and other similar methods, showed

CORRESPONDENCE Jinha Jung jinha@purdue.edu Lyles School of Civil Engineering, Purdue University, West Lafayette, IN 47906, USA

that the area of aggregate exposed by a cross-sectional cut could be an accurate predictor of larger sieve gradation. However, the procedure used was destructive to the sample (Yue et al., 1995; Bruno et al., 2012).

More recent research into image analysis of asphalt cores has either experimented with different sensors for capturing images or focused on the algorithms used to process the images. In 2017, Obaidat et al. photographed core slices with a cellphone instead of a flatbed scanner (2017), and in 2014, Vadood et al. introduced an approach for detecting both fine and coarse aggregate gradation using a ratio between the color bands of digital images of core slices (2014). Tielmann and Hill's work published in 2018 used flatbed scanners to capture images for studying air voids in asphalt. Instead of cutting the core across its length to form disks, the asphalt cores were cut along their length, and the cut surfaces were polished and filled with fluorescent material to improve contrast in the imaging (Tielmann and Hill, 2018). All the past image analysis methods have damaged the sample to obtain a cross-sectional image of the core.

Other properties of asphalt cores have also been studied using image processing techniques. in 2013, Levenberg and Manevich outlined a process for determining the bulk density of an asphalt core based on a three-dimensional mesh model reconstructed from images using standard photogrammetric procedures. The images were taken from a stationary, consumer-grade camera and the core was set on a turntable and manually rotated between each image. The goal of this research was to calculate the volume of the core. No attempts were made to determine aggregate size (Levenberg and Manevich, 2013).

In parallel with the image processing methods of analyzing the distribution of aggregates within the asphalt core sample, other methods have been introduced. X-ray Computed Tomography has been developed to capture images of asphalt cores. These images have been used to map the three-dimensional changes in material density and analyze the distributions of aggregate and air voids in the bituminous binder (Tashman et al., 2007; Zelelew and Papagiannakis, 2011; Farcas, 2012; Xing et al., 2019; du Plessis and Boshoff, 2019). While the results of X-ray technology have been accurate, the main limitation of X-ray CT is that the equipment is expensive and therefore not readily available (Obaidat et al., 2017). Further, ultrasonic wave transmission has been used with some success to quantify air pockets in asphalt samples (Zargar and Bullen, 2021) and to evaluate the strength quality of pavement (Kadium and Sarsam, 2020). Indentation testing is another method for evaluating asphalt pavement advertised as being quasi-non-destructive. While it does not quantify the aggregate gradation directly, it can be used to make assumptions about the gradation in thin layers of pavement (Fadil et al., 2022).

To overcome the limitations of the previous studies used to analyze asphalt cores, the main objectives of this study are: 1) to develop a non-destructive method for asphalt core analysis; 2) to develop an automated algorithm detecting layer boundaries; and 3) to develop an automated algorithm to classify aggregate mixture gradation.

2. Material and Methods

2.1 Material

Six asphalt cores are used in this research. Two cores (*Roadway_A* and *Roadway_B*) were drilled from existing roadways and are 10 cm in diameter and 30cm in length exhibiting five layers. The remaining four cores are small mix validation cores. These cores were drilled from test mixes with known aggregate gradations and are 4 cm in diameter and 10 cm in length. Two of the validation cores contain aggregate gradations classified as 9.5 mm (*9.5_A* and *9.5_B*), and the other two validation cores contain aggregate gradations classified as 19.0 mm (*19_A* and *19_B*). The workflow of the proposed methodology is illustrated in Fig. 1.

2.2 Close-Range Photogrammetry-Based 3D Scanning

Accurate image analysis requires a distortion-free image. In past research, a distortion-free image was acquired by first cutting the core to create a flat surface and then scanning that flat surface with a flatbed scanner. In this project, the goal is to develop a non-destructive process, so only the cylindrical face of the core is available for imaging. To do this, an image must be produced which removes any distortion caused by the curved surface. We developed the following process for producing a distortion-free image of the surface: first, photos of the surface of the core were captured with a digital camera; second, photogrammetric techniques were employed to reconstruct a three-dimensional point cloud capturing the color and texture of the core surface; third, a mapping prescription was applied to "unroll" or map the cylindrically shaped

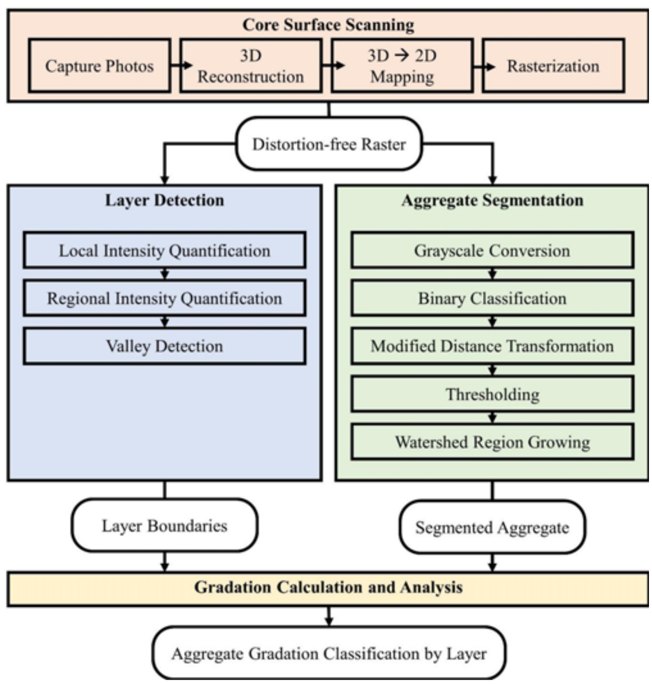

Fig. 1. Flow Chart Showing the Processing Steps of Our Proposed Non-Destructive Layer and Gradation Classification Methodology

point cloud to a planar representation of the core's surface; lastly, the planar point cloud was rasterized to create a two-dimensional image of the core's surface.

2.2.1 Data Collection

The first step in creating the required image was to photograph the asphalt core using a digital camera. The core was set on a turntable and a Sony a7 MarkII DLSR camera captured photos every 15 degrees around the core at a resolution of 5304px by 7952px. A small aperture (f/22) was maintained to create the largest depth of field possible during the image capture process. This allowed the surface of the core to remain in focus even as the surface curves away from the camera. Using a turntable allowed the camera to remain stationary, keeping the interior orientation parameters consistent between exposures. It also allowed the core to be illuminated with the same lighting conditions in every photograph. Fig. 2 shows the data collection setup.

2.2.2 Structure from Motion for 3D Reconstruction

After photographing the core, the second step was to create a three-dimensional point cloud of the core. Agisoft's Metashape implemented structure-from-motion (SFM) techniques to find common points between the photos and complete the three-dimensional reconstruction. This method of reconstruction produced a scaleless point cloud of the core. For each point in the cloud, Metashape assigned a color value extracted from the photographs. The point clouds for the two roadway cores contained about twenty-five million points while each of the validation cores was modeled with about four million points. To scale the point cloud, four of Metashape's circular pattern targets were printed on a piece of paper and placed on the turn table prior to imaging the core. The circular targets were each approximately 2 cm in diameter and were placed at the corners of a 14 cm × 14 cm square. During imaging, the core was set in the center of the square formed by these four targets, as seen in Fig. 2. These targets were then present in the reconstructed point cloud and used in Metashape to define the origin and scale of the point cloud. Finally, the point cloud was exported from Metashape in the las format and imported into a Python environment for further processing.

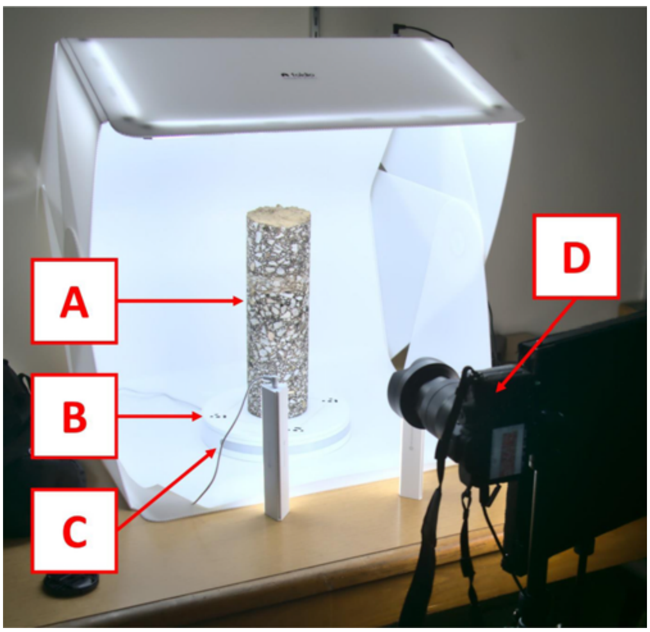

Fig. 2. The Experimental Environment: A – Sample Set in the Photo Booth, B – 14 cm × 14 cm Printed Square with Metashape Targets at Each Corner for Scaling the SFM Point Cloud, C – Turntable Used for Controlled Rotation of the Sample During Imaging, D - Sony a7 MarkII DLSR Camera

2.2.3 Coordinate Transformation

The third step required the cylindrical point cloud to be mapped to a planar surface. Before a mapping prescription could be applied, the central axis of the core had to be aligned with the z-axis of the point space through a similar coordinate transformation. Fig. 3 illustrates the effect of applying the transformation expressed through the following equation:

$$p_i^b = -t + R_a^b p_i^a, \tag{1}$$

where p_i^a represents the coordinate vector of the ith point after transformation into the b coordinate frame; t is the intercept of the axis of the core, before transformation, with the x-y plane of the a coordinate space as shown in Fig. 3(a); R_a^b is the three-dimensional rotation matrix that rotates a point p_i^a in the unaligned coordinate frame a to its new position p_i^b in the aligned coordinate frame b, and p_i^a is the coordinate vector of the ith point in the original a coordinate frame. The x-y intercept of the core axis t and the direction of the axis $\bar{u}$ was found using a least squares line fitting procedure. A random selection of points from the core was used as inputs to the least squares procedure. The points from the top and bottom one centimeter of the core were not considered for random selection to exclude the noise found at the extremities of the point cloud. The intercept t was directly used in the transformation, and the direction vector $\bar{u}$ was used in a Rodrigues rotation formula to solve for the rotation R_a^b. Fig. 3(b) illustrates the new alignment of the core after transformation.

Following the transformation, a mapping prescription was applied which transformed the cylindrical point cloud into a planar point cloud. Fig. 4 shows the relationship between the

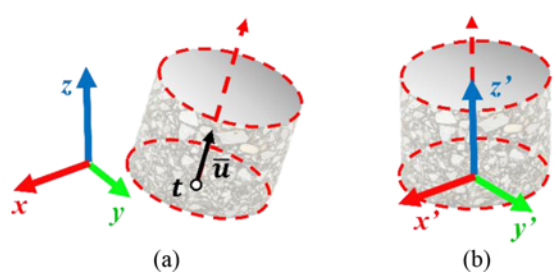

Fig. 3. Aligning the Central Axis of the Core to the Z-Axis of the Space: (a) The Point Cloud of the Core Prior to Coordinate Transformation, (b) The Point Cloud of the Core after Coordinate Transformation

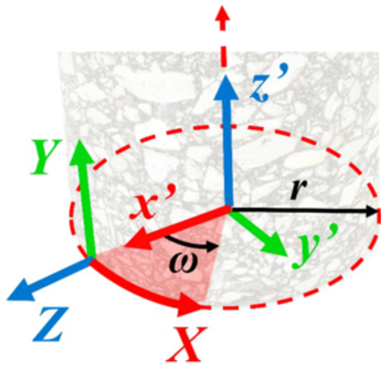

Fig. 4. The Relation between the Cylindrical Point Cloud Coordinates (x', y', z') and the Planar Mapping Coordinates (X, Y, Z)

cylindrical point cloud coordinates and the planar coordinates of the mapping. The details of the mapping are expressed in the following equations:

$$X = \omega r\,, \tag{2}$$

$$Y = z\,, \tag{3}$$

$$Z = \sqrt{x'^2 + y'^2} - r\,, \tag{4}$$

where X, Y, Z represent the coordinates of the point cloud after the mapping, r is the average distance of all points from the central axis of the core, and ω is the angle from the x-axis, in the xy-plane, to the point of interest. The result of this mapping was a planar point cloud where the X-coordinate represented the longitudinal distance along the surface of the core, the Y-coordinate represented the distance from the bottom of the core, and the Z-coordinate represented the distance of a given point from the best-fit cylindrical approximation of the core.

2.2.4 Distortion-Free Raster Image Generation

The fourth and final step to creating the distortion-free image for image analysis was to rasterize the planar point cloud. A Python script cycled through all points in the planar point cloud addressing each point to a raster grid cell based on the point's position. The color for each raster grid was found by averaging the band intensity value of every point addressed to a given raster cell. The resulting RGB raster for core *Roadway_A* can be seen in Fig. 5. An additional raster was created using the average z coordinate of all points assigned to a given cell. This raster shows how the texture of the core deviates from a perfect cylinder as shown in Fig. 5.

2.3 Layer Detection

When building an asphalt road, each layer of asphalt is spread out, compacted, and coated in a thin layer of tar before the next layer is laid down. This process often causes the interface between two layers of asphalt to appear as a thin line of binder running perpendicular to the central axis of the core. The layer detection algorithm in this paper attempts to detect this linear feature in the image.

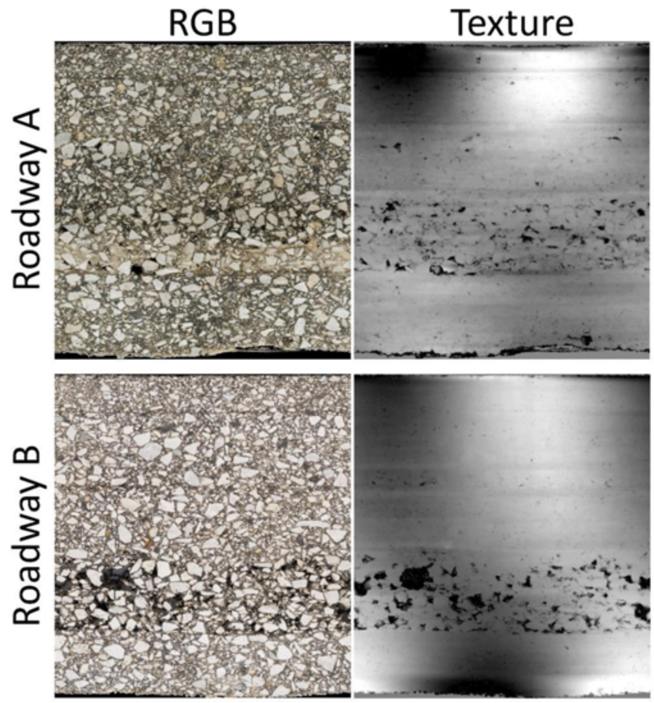

Fig. 5. RGB and Texture Images of Both Roadway_A and Roadway_B

Figure 6 shows the layer detection process as applied to core *Roadway_A*. A moving window with the x-dimensions equal to the total number of columns in the surface image and a y-dimension equal to 1% of the total number of rows in the surface image was used to calculate an average local intensity value of the red band for every row in the surface image. In this experiment, the average cell size of the distortion-free raster was 0.1 mm. The core used to build the algorithm had an open grade layer that collected light-colored sediment. To correct for regional intensity changes, a trend line was calculated using the same moving window method. The y dimension of this second moving average was 20% of rows. The trend value for each row was subtracted from the average intensity of the row. This corrected for regional changes in brightness. Through trial and error, one standard deviation was used as a threshold value to identify valleys (dark rows) that corresponded with layer interfaces in the asphalt core, Fig. 7 shows the layers detected above plotted onto the surface image of core *Roadway_A*.

To validate this method, the algorithm applied was applied to core *Roadway_B*. Core *Roadway_B* had several black pits in the surface where aggregate had fallen out after the core was drilled. These cavities revealed large areas of the dark binder. The algorithm described above presumes that the layer interfaces will be the darkest rows; however, these cavities invalidated this presumption. Fig. 8 shows the results of the algorithm plotted on the surface image of *Roadway_B*. Visual inspection shows that the algorithm failed to correctly identify layer divisions in the second core. Adding more parameters to the layer detection would make this task more robust. A good starting point for future work would be to incorporate the surface texture image created during the

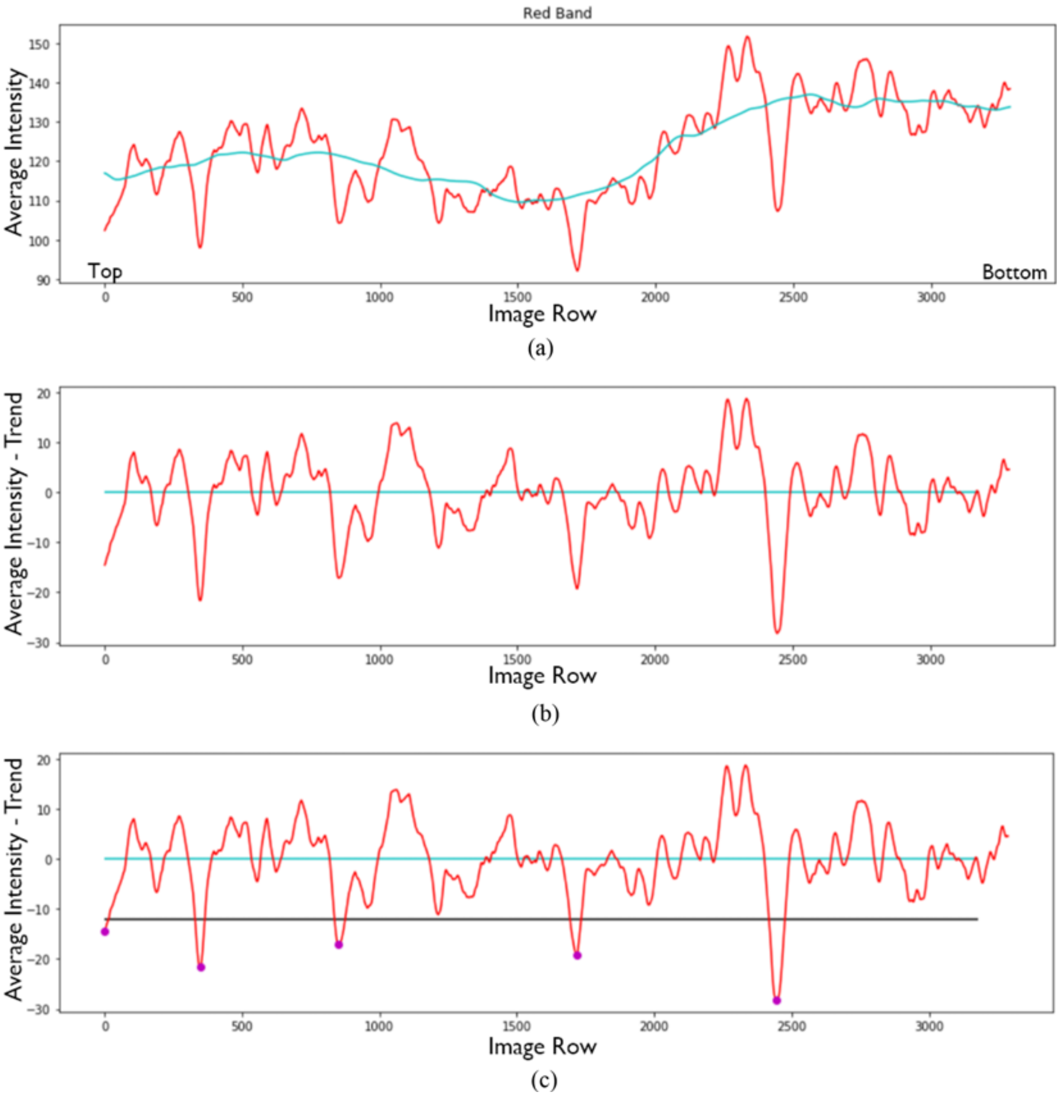

Fig. 6. Layer Detection Steps Using the Red Band of the RGB Surface Image of Core *Roadway_A*: (a) First, a Moving Window of 1% of Pixel Rows is Used to Calculate Average Intensity (red line) While a Moving Window of 20% of Pixel Rows is Used to Calculate Trend Line (blue line), (b) Next, the Trend is Subtracted from the Average Intensity for Each Row, (c) Finally, Valleys Below One Standard Deviation from the Trend are Identified as Layer Divisions

reconstruction process. This image identifies changes in the porosity of the core which could be used to indicate a layer change.

2.4 Aggregate Segmentation

Before beginning to estimate aggregate size, the areas of a surface image belonging to individual aggregates must be identified. The following steps for aggregate segmentation were followed: first, the three bands of the RGB surface image were combined into a single grayscale image; second, the grayscale image was binarized to distinguish between aggregate and binder; finally, individual aggregates were identified through a watershed algorithm.

2.5 Image Conversion

The first step was to create a grayscale image from the bands of the RGB image. This was accomplished by implementing the luminance method of converting an RGB image to grayscale – the most common method offered in photo manipulation software. This method attempts to preserve the brightness perceived in the color image through a weighted combination of the RGB channels as expressed in Eq. (5) (Kanan and Cottrell, 2012).

$$G = 0.3R + 0.59G + 0.11B\,, \tag{5}$$

where G is the intensity value of the resulting pixel in the grayscale image, and R, G, B are the intensity values of the red, green, and blue bands respectively.

2.5.1 Binary Classification

With the grayscale image created, the second step was to binarize to distinguish between aggregate and binder. Fig. 9 shows the distribution of the intensity values in the grayscale image. The

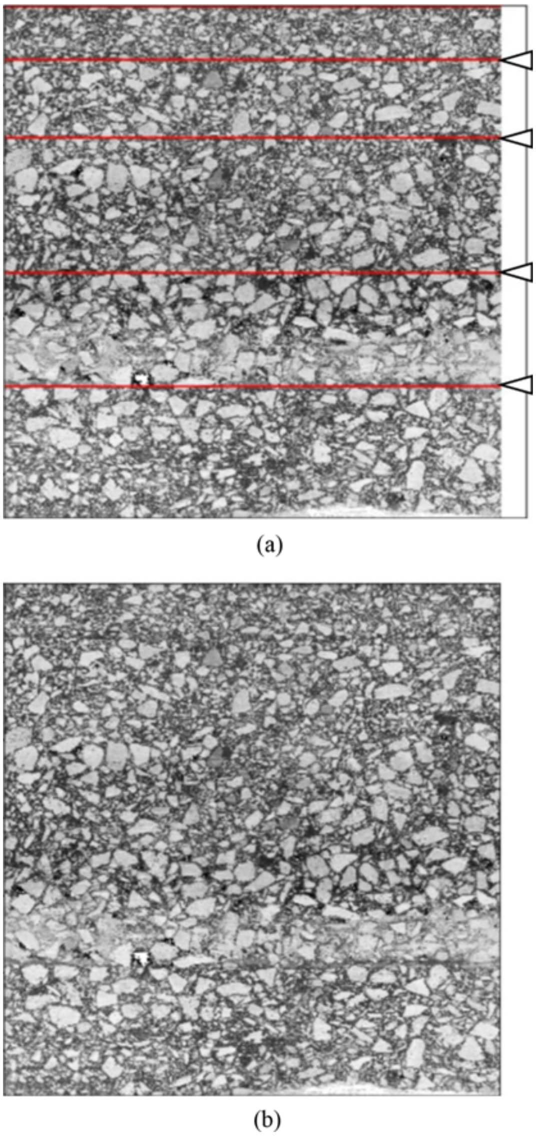

Fig. 7. Layer Detection Results for *Roadway_A*: (a) *Roadway_A* Surface Image with Detected Layers in Red, (b) *Roadway_A* Surface Image for Reference (Arrows indicate actual layer interfaces.)

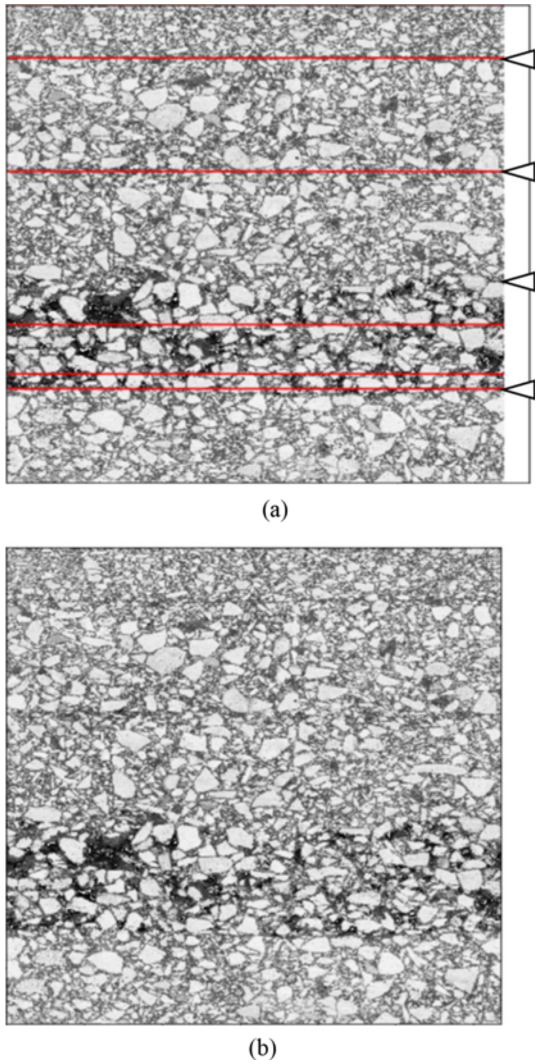

Fig. 8. Layer Detection Results for *Roadway_B*: (a) *Roadway_B* Surface Image with Detected Layers in Red, (b) *Roadway_B* Surface Image for Reference (Arrows indicate actual layer interfaces.)

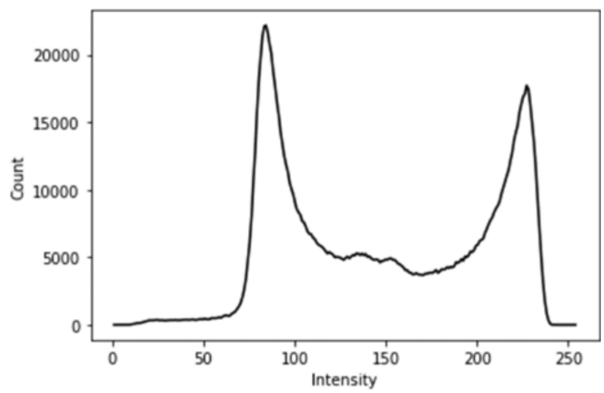

Fig. 9. Distribution of Intensity Values in the Grayscale Image

bimodal distribution seen in Fig. 9 indicates high contrast between binder and aggregate. To find the best threshold value between the two peaks for binarization, a simple Otsu thresholding technique was implemented, a method which has precedence in the literature (Shi et al., 2020). This threshold value was then used to segment the image into aggregate and binder. The result can be seen in Fig. 10(b).

Once again, the sediment in the open grade layer hindered the distinction between aggregate and binder. Because of the lightness of the sediment, much of the binder was miss-labeled as aggregate. Past research focused on small portions of the core which have been carefully cut and cleaned prior to imaging. But since this method is designed for nondestructive testing, the discoloration due to sediment buildup within the open pores of the pavement could not be ignored. For these reasons, the global threshold binarizing process was abandoned.

Instead of a global threshold, an adaptive threshold was used. The adaptive threshold uses the average intensity of a window of pixels as the threshold for the central pixel in the window.

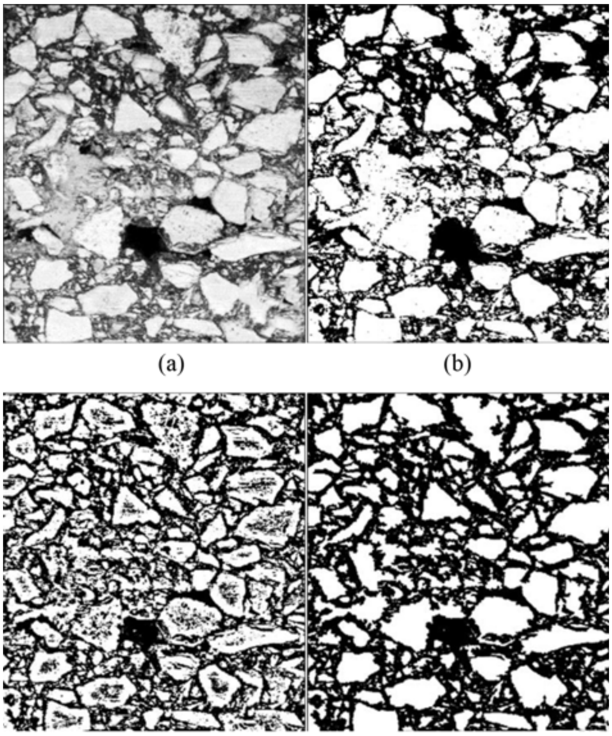

(a) (b) (c) (d)

Fig. 10. A Portion of the Core Surface Image where Sediment Build-Up Made Aggregate Segmentation Difficult: (a) The Grayscale Image, (b) The Binarized Image Based on the Otsu Threshold Showing Poor Aggregate Definition, (c) A Binarized Image after the Application of the Adaptive Threshold, (d) A Binarized Image after the Application of the Adaptive Threshold Followed by a Cleaning Routine

Through trial and error, it was determined that a window of 51 pixels by 51 pixels (or about 5 mm × 5 mm in object space) would be used to calculate the threshold value for the central pixel. This window size was chosen because it was a useable balance which minimized mislabeling small darker aggregate, or the centers of large aggregate, as binder. Though this window size was determined by experimentation, it is useful to note that the resulting 5 mm square approximates the average median sieve size. In other words, for most of the gradation curves, roughly 50% of the aggregate by weight should pass through a 5 mm sieve. The results of this adaptive thresholding process can be seen in Fig. 10(c). Inspection of Fig. 10(c) shows black splotches in the center of a larger aggregate. These splotches are an artifact of the adaptive thresholding process. As the window passes over the center of a large aggregate, the average intensity value of the pixels in the window rise, subjecting the target pixel to a much higher threshold value. Since the binder surrounds the aggregates, pixels correctly labeled as binders (black pixels) are interconnected. A simple script that performs morphological operations was written to remove the isolated black patches. The resulting binarized image can be seen in Fig. 10(d).

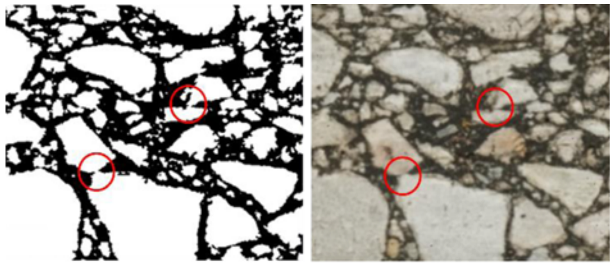

(a) (b)

Fig. 11. Connected Aggregate in the Binarized Image: (a) Binarized Image with Connected Aggregate Circled in Red, (b) RGB Image for Reference

2.5.2 Aggregate Segmentation

The final step to segment the image was to label individual aggregate. The binarized image could not be used directly to identify individual aggregate. Fig. 11 shows an initial problem with identifying individual aggregate – some of the aggregate are connected. Vadood et al. (2014) suggest a method for separating connected aggregates which, first, applies a distance transform then thresholds the binarized image to shrink the boundaries of each aggregate, then implements a watershed algorithm to grow the aggregate boundaries back to their proper position. Here, this general process will be followed with some modifications to the distance transform.

To shrink the size of each aggregate, a threshold was applied to a modified distance transform of the binarized image. A normal distance transform colors each white pixel in a binarized image by the distance from that pixel to the nearest black pixel. Applying a threshold to a normal distance transform directly has the effect of shrinking each aggregate by a fixed number of pixels. For many small aggregates, this fixed shrinking would erase the aggregate completely. To avoid erasing aggregate, a script was written that iterated through each aggregate in the binary image. For each aggregate, a distance transform was applied and the value of the brightest pixel after the transformation was selected. Based on the brightest pixel, a scale factor was calculated which would scale all values in the aggregate to range between 0 and 255. The modified distance transform produced an image where the center of each aggregate – no matter how small – had an intensity value of 255, as shown in Fig. 12(b). A threshold was then applied to this modified distance transform image to shrink the boundaries of each aggregate proportionately to their size. This new binary image identified the parts of the image which were sure to be individual aggregates, as shown in Fig. 12(c).

Each separate aggregate was labeled and then a watershed algorithm was used to grow the boundaries of each aggregate based on the intensity value of the grayscale image. In the resulting image, each color represents an individual aggregate. Refer to Fig. 12(d). Visual comparison between the final segmented image and the core itself showed remarkable fidelity to the original core.

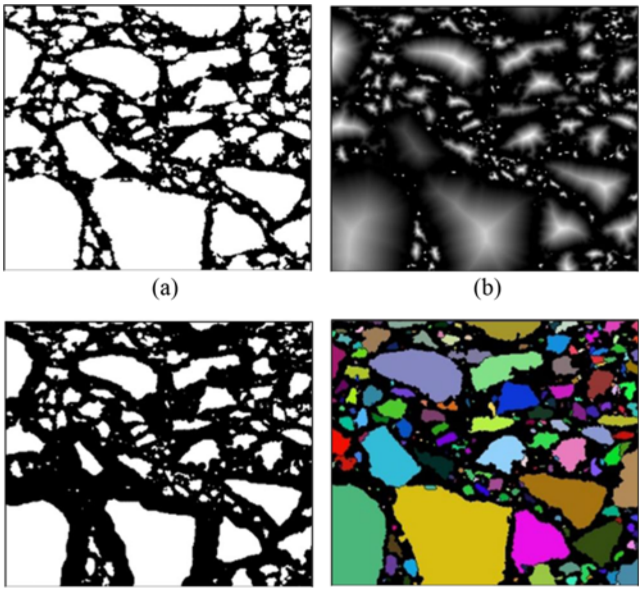

Fig. 12. Pictorial Flow Chart of the Aggregate Labeling Process: (a) The Results of Adaptive Binarization and Cleaning, (b) The Modified Distance Transformation Changes the Slope of the Gradation Based on the Size of the Aggregate, (c) The Results of Applying a Threshold to the Distance Transformed Image who the Center Portions of Each Aggregate as White Blobs, (d) After Applying a Watershed Algorithm, the Boundaries of Each Aggregate are Defined, and Each Aggregate is Labeled Uniquely (represented by random colors.)

2.6 Gradation Calculation

As discussed at the beginning of this paper, the asphalt mixture is made up of a blend of different size aggregates. The specific blend of aggregates is called the gradation. Each gradation is given a classification label based on the percentages of aggregate sizes in the mixture. A sieve test is the standard way to determine the gradation of any mix of gravel. A series of sieves with successively larger holes are stacked into a machine and the aggregate mixture is placed on the top sieve. Then the stack is agitated. After agitation, the percentage of the mixture, by weight, passing through each sieve is measured. When plotted on a chart where the x axis represents the sieve size and the y axis indicates the percentage of material passing each sieve size, a cumulative distribution curve is created. Fig. 13 shows the known gradation curve of the two 9.5 mm validation cores, and Fig. 14 shows the known gradation curve of the two 19.5 mm validation cores.

This section will detail the method employed to determine the gradation of the aggregate mixture captured by the segmented image. In the mechanical gradation process, percentages are determined by the weight of the aggregate. Here percentages are determined by image area. Following the work of Vadood et al., the percentage passing each sieve size was calculated with Eq. (6) (2014):

$$P_i = \frac{A_i}{A_t} * 100\% , \tag{6}$$

where P_i is the percentage of aggregates passing the i^{th} sieve, A_i is the sum of the area of all aggregate passing the i^{th} sieve, and A_t is the sum of the areas of all aggregates.

Using the ratio of areas is the method used in almost all the literature reviewed. However, there are differences in which shape parameter should be used when determining if an aggregate passes a given sieve (Vadood et al., 2014; Maiti et al., 2017). To determine if a given aggregate would pass through a given sieve size, the following three descriptors of shape were calculated for each segmented aggregate: major axis of the best fit ellipse, minor axis of the best fit ellipse, and equivalent diameter (the

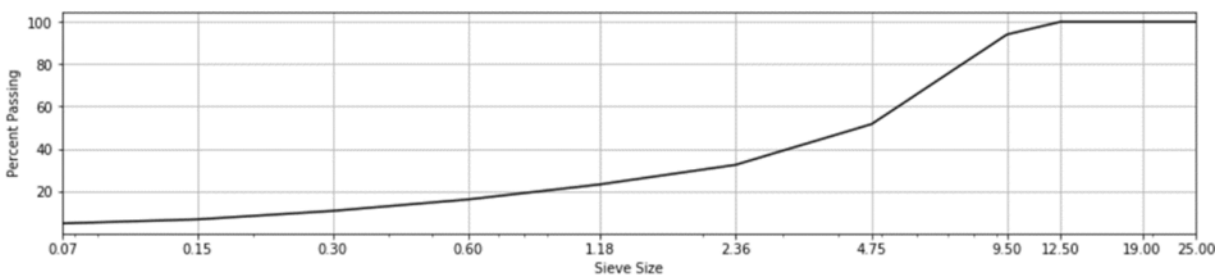

Fig. 13. Known Gradation Curve for the Two 9.5 mm Validation Cores Used in This Research, Cores *9.5 mm_A* and *9.5 mm_B*

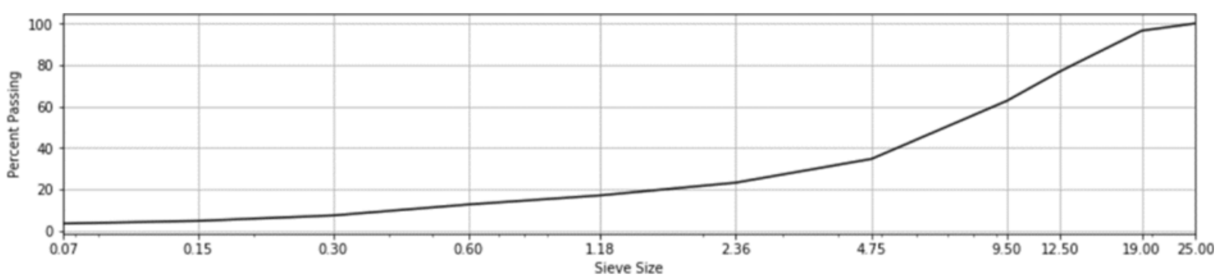

Fig. 14. Known Gradation Curve for the Two 19 mm Validation Cores Used in This Research, Cores 19 mm_A and 19 mm_B

Table 1. RMSE Values (units of 'percent passing') are Used to Compare Gradation Curves Calculated Using Three Different Shape Descriptors to the Known Gradation Curve

Core	Major Axis	Minor Axis	Equivalent Diameter
9.5 mm_A	10.6	8.3	6.9
9.5 mm_B	8.5	10.7	7.5
19 mm_A	8.7	11.4	7.5
19 mm_B	6.2	14.0	10.9

diameter of a circle with the same area as the aggregate). With each of these measures of shape, a gradation curve was calculated for each of the four validation cores. The RMSE value was determined between each calculated curve and the known distribution. These RMSE values can be found in Table 1. Note that RMSE values are in units of percent passing. These RMSE values are calculated to determine which shape parameter yields the best approximation to the known gradation curve, they are not intended to indicate the accuracy of the proposed gradation method. For this reason, the magnitude of the RMSE values is meaningful only in comparison with each other. From this analysis, it is seen that equivalent diameter is the descriptor of shape which produces the lowest RMSE, indicating that the gradation curve generated using the equivalent diameter descriptor most closely resembles that of the known gradation. For the remainder of this paper, the equivalent diameter will be used as the shape descriptor used to determine if a given aggregate passes through a given sized sieve.

3. Results and Discussion

This section of the paper will be broken into two parts. First, it will discuss the method used to classify a gradation curve according to the INDOT specifications and will show the results of classifying the four validation cores. Second, this section will apply the gradation test to each layer of a multilayer core to demonstrate how this process might be used to determine the gradation of each layer within a roadway sample.

As mentioned above, each mix of aggregate is classified based on the gradation of aggregates. Table 2 shows the standards which the Indiana Department of Transportation uses to classify a specific gradation. For all four validation cores, a gradation curve was calculated using the process outlined above. That gradation curve was then classified based on the INDOT specifications. For each classification, Table 2 shows the range of percentages of each aggregate size that should exist in the mix. Too few validation cores were available to build and test a rigorous classification procedure, so a simple scoring system was employed to determine which of the INDOT classifications best fit the calculated gradation curves. Table 3 shows the point system.

Table 3. Points Awarded to a Gradation for Passing Each INDOT Specification Listed in Table 2

Points Awarded for Passing the Test Listed in the INDOT Specifications					
	25.0 mm	19.0 mm	12.5 mm	9.5 mm	4.75 mm
Sieve Size					
50.0 mm					
37.5 mm	1				
25.0 mm	1	1			
19.0 mm	2	1	1		
12.5 mm		2	1	1	1
9.5 mm			2	1	1
4.75 mm				2	1
2.36 mm	1	1	1	1	
1.18 mm					1
600 µm					
300 µm					
75 µm	1	1	1	1	1

Table 2. INDOT Specifications for Gradation Classification (INDOT, 2022)

Dense Graded, Mixture Designation – Control Point (Percent Passing)					
	25.0 mm	19.0 mm	12.5 mm	9.5 mm	4.75 mm
Sieve Size					
50.0 mm					
37.5 mm	100.0				
25.0 mm	90.0 – 100.0	100.0			
19.0 mm	< 90.0	90.0 – 100.0	100.0		
12.5 mm		< 90.0	90.0 – 100.0	100.0	100.0
9.5 mm			< 90.0	90.0 – 100.0	95.0 – 100.0
4.75 mm				< 90.0	90.0 – 100.0
2.36 mm	19.0 – 45.0	23.0 – 49.0	28.0 – 58.0	32.0 – 67.0*	
1.18 mm					30.0 – 60.0
600 µm					
300 µm					
75 µm	1.0 – 7.0	2.0 – 8.0	2.0 – 10.0	2.0 – 10.0	6.0 – 12.0

Core_9.5mm_A Layer1 108.5mm Thick — Specification Test

Sieve Size	Cnt	Calc %	Known %	25.0mm	19.0mm	12.5mm	9.5mm	4.75mm
1.5 37.50mm	0	100.0	100.0	PASS	----	----	----	----
1 25.00mm	0	100.0	100.0	PASS	PASS	----	----	----
3/4 19.00mm	0	100.0	100.0	FAIL	PASS	PASS	----	----
1/2 12.50mm	0	100.0	100.0	----	FAIL	PASS	PASS	----
3/8 9.50mm	4	95.2	94.0	----	----	FAIL	PASS	PASS
4 4.75mm	76	58.6	51.7	----	----	----	PASS	FAIL
8 2.36mm	237	27.0	32.4	PASS	PASS	FAIL	FAIL	----
16 1.18mm	485	11.4	23.2	----	----	----	----	FAIL
30 0.60mm	820	4.2	16.1	----	----	----	----	----
50 0.30mm	1391	0.9	10.7	----	----	----	----	----
100 0.15mm	1377	0.1	6.7	----	----	----	----	----
200 0.07mm	348	0.0	4.8	FAIL	FAIL	FAIL	FAIL	FAIL
RMSE between "Calc" and "Known": 6.6				3	3	2	4	1

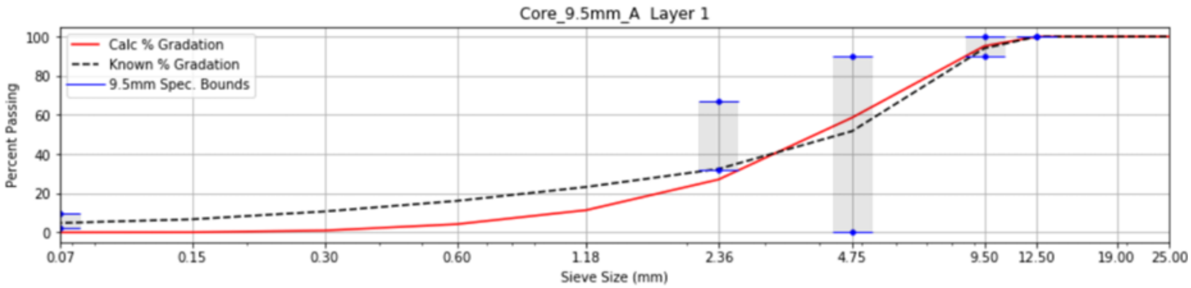

Fig. 15. The Results of the Gradation Testing Method Detailed in This Paper Prepared for Core 9.5 mm_A (The gradation classification method correctly classified the aggregate as 9.5 mm.)

Core_9.5mm_B Layer1 109.2mm Thick — Specification Test

Sieve Size	Cnt	Calc %	Known %	25.0mm	19.0mm	12.5mm	9.5mm	4.75mm
1.5 37.50mm	0	100.0	100.0	PASS	----	----	----	----
1 25.00mm	0	100.0	100.0	PASS	PASS	----	----	----
3/4 19.00mm	0	100.0	100.0	FAIL	PASS	PASS	----	----
1/2 12.50mm	0	100.0	100.0	----	FAIL	PASS	PASS	----
3/8 9.50mm	1	98.8	94.0	----	----	FAIL	PASS	PASS
4 4.75mm	69	66.7	51.7	----	----	----	PASS	FAIL
8 2.36mm	240	32.6	32.4	PASS	PASS	PASS	PASS	----
16 1.18mm	538	14.2	23.2	----	----	----	----	FAIL
30 0.60mm	1038	4.7	16.1	----	----	----	----	----
50 0.30mm	1511	1.0	10.7	----	----	----	----	----
100 0.15mm	1501	0.1	6.7	----	----	----	----	----
200 0.07mm	445	0.0	4.8	FAIL	FAIL	FAIL	FAIL	FAIL
RMSE between "Calc" and "Known": 7.2				3	3	3	5	1

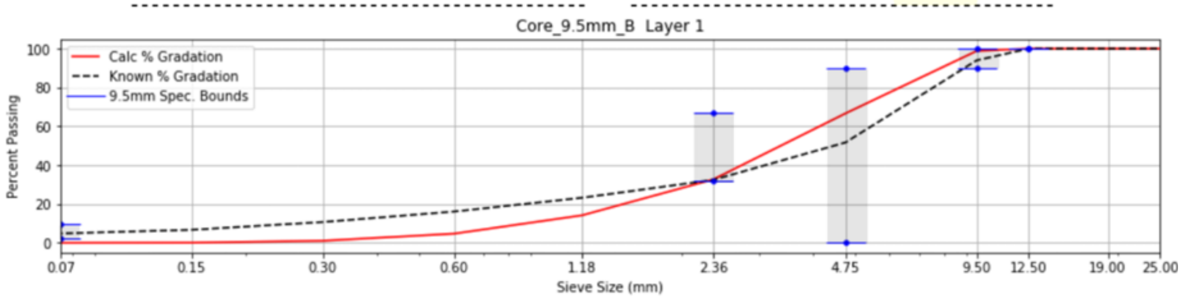

Fig. 16. The Results of the Gradation Testing Method Detailed in This Paper Prepared for Core 9.5 mm_B (The gradation classification method correctly classified the aggregate as 9.5 mm.)

The calculated gradation curve for each of the four validation cores was tested against the INDOT specifications. The gradation curve was assigned the classification which earned the largest number of points.

Figures 15 – 18 show the output of the gradation classification process. The table in the top left of the figures shows the number of aggregates ("Cnt"), the calculated percentage passing ("Calc %"), and the known percentage passing ("Known %") for each sieve size. The table on the top right indicates how the calculated gradation curve matched the INDOT specification shown in

Core_19mm_A Layer1 108.6mm Thick — Specification Test

Sieve Size	Cnt	Calc %	Known %	25.0mm	19.0mm	12.5mm	9.5mm	4.75mm
1.5 37.50mm	0	100.0	100.0	PASS	----	----	----	----
1 25.00mm	0	100.0	100.0	PASS	PASS	----	----	----
3/4 19.00mm	0	100.0	96.5	FAIL	PASS	PASS	----	----
1/2 12.50mm	5	89.1	76.9	----	PASS	FAIL	FAIL	----
3/8 9.50mm	12	74.0	62.6	----	----	PASS	FAIL	FAIL
4 4.75mm	81	35.5	34.6	----	----	----	PASS	FAIL
8 2.36mm	157	15.8	23.1	FAIL	FAIL	FAIL	FAIL	----
16 1.18mm	282	7.3	17.0	----	----	----	----	FAIL
30 0.60mm	591	2.8	12.6	----	----	----	----	----
50 0.30mm	992	0.7	7.3	----	----	----	----	----
100 0.15mm	1151	0.1	4.7	----	----	----	----	----
200 0.07mm	482	0.0	3.4	FAIL	FAIL	FAIL	FAIL	FAIL
RMSE between "Calc" and "Known": 7.1				2	4	3	2	0

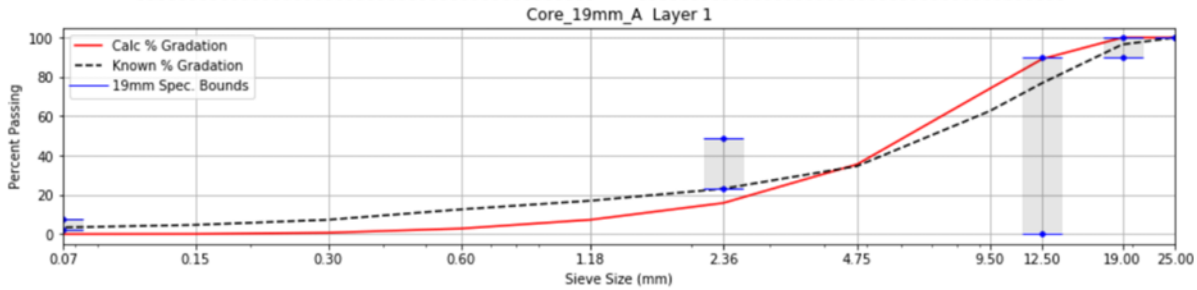

Fig. 17. The Results of the Gradation Testing Method Detailed in This Paper Prepared for Core 19 mm_A (The gradation classification method correctly classified the aggregate as 19 mm.)

Core_19mm_B Layer1 109.1mm Thick — Specification Test

Sieve Size	Cnt	Calc %	Known %	25.0mm	19.0mm	12.5mm	9.5mm	4.75mm
1.5 37.50mm	0	100.0	100.0	PASS	----	----	----	----
1 25.00mm	0	100.0	100.0	PASS	PASS	----	----	----
3/4 19.00mm	0	100.0	96.5	FAIL	PASS	PASS	----	----
1/2 12.50mm	1	97.6	76.9	----	FAIL	PASS	FAIL	----
3/8 9.50mm	8	86.2	62.6	----	----	PASS	FAIL	FAIL
4 4.75mm	86	44.5	34.6	----	----	----	PASS	FAIL
8 2.36mm	186	21.4	23.1	PASS	FAIL	FAIL	FAIL	----
16 1.18mm	396	9.4	17.0	----	----	----	----	FAIL
30 0.60mm	723	3.5	12.6	----	----	----	----	----
50 0.30mm	1191	0.8	7.3	----	----	----	----	----
100 0.15mm	1217	0.1	4.7	----	----	----	----	----
200 0.07mm	449	0.0	3.4	FAIL	FAIL	FAIL	FAIL	FAIL
RMSE between "Calc" and "Known": 10.5				3	2	4	2	0

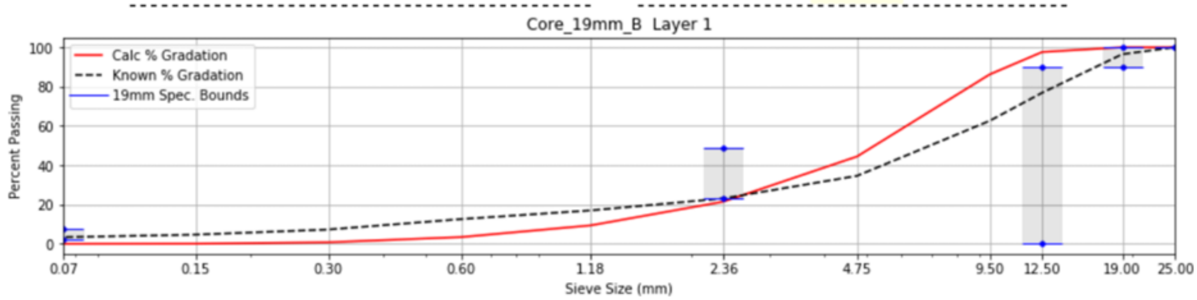

Fig. 18. The Results of the Gradation Testing Method Detailed in This Paper Prepared for Core 19 mm_B (The gradation classification method incorrectly classified the aggregate as 12.5 mm.)

Table 2. The column highlighted in yellow indicates which classification the gradation curve has been assigned. The graph at the bottom presents the data from the two tables graphically. The known gradation curve is drawn in a dashed line and the calculated gradation curve is drawn in solid red. The gray areas of the graph illustrate ranges specified by the INDOT specifications for the assigned aggregate classification.

The output from the gradation test shows that even with a simplistic classification procedure the gradation process successfully classified three of the four cores – an accuracy of 75%. Cores 9.5 mm_A, 9.5 mm_B, and 19 mm_A were classified correctly as 9.5 mm, 9.5 mm, and 19 mm aggregate mix respectively. 19 mm_B was incorrectly classified as 12.5 mm aggregate mix.

There are a few limitations of this study. First, as indicated by the gradation curves in Figs. 15 – 18, the aggregate less than 2.5 mm are underrepresented in the distribution; and an aggregate less than 0.1 mm is not represented at all. This underestimation of small aggregates affects the results of the gradation classification. The INDOT specifications list a narrow window of allowable passing percentages for the 2.36 mm aggregate size. However, since this size of aggregate is underestimated in our image processing method, our results often indicate that the mix contains less of the small aggregates than is present in the known gradation curve. Part of this underestimation can be attributed to the resolution of the RGB core surface image. The density of the point cloud used to create the surface image only allowed an image resolution of 0.1 mm. Grains smaller than this resolution could not be detected. The failure of our method to detect grains between 0.1 mm and 2.5 mm in the correct proportions indicates that the number of small grains visible on the cut surface of the core is not representative of the quantity of grains within the mix. Small grains are much more fragile than larger aggregate, so during drilling and handling the core, small grains are split, smudged over with bitumen, or lost reducing their representation on the surface of the core.

A related problem exists for the largest aggregate sizes. As shown in Fig. 18, core 19 mm_B was incorrectly classified as 12.5 mm aggregate mix because 100% of the aggregate passed through the 12.5 mm sieve size. Given that the other 3 cores had their gradation correctly classified, we do not see the failure of core 19 mm_B to indicate a flaw in our image processing. Rather, this failure indicates that large aggregate simply did not show a large surface area on the cut surface of the core. In our proposed method, the size of the aggregate is determined by the cut surface area of the aggregate on the face of the core. The percent passing measure is determined by the sum of the areas of specific aggregate sizes (Eq. (6)). Since large aggregate can exhibit large amounts of surface area when compared to the smaller aggregates sizes, each individual large aggregate has a relatively large impact on the percentage passing value for its sieve size. This makes estimating the percentage passing the larger sieve sizes highly dependent on the size of the cut surface of only a few individual stones exposed on the surface of the core. For core 19 mm_B, we hypothesize that, by random chance, no large aggregate were positioned in the mix such that the drilling process revealed a large cross section. Thus, our method overestimated the percentage of the aggregate that would pass the 12.5 mm sieve size and incorrectly classified the aggregate gradation.

Both problems listed above – underestimating the percentage of small aggregate and failing to detect larger aggregate – could potentially be corrected by including of a few parameters into the percent passing calculation which would adjust for known misrepresentation of specific aggregate sizes. Discovering these parameters would require significantly more than four samples. This leads to the last major limitation of this study. Only four cores of known gradation were available for testing. Though we have successfully shown that correct gradation classification is easily achievable using distortion-free images of the drilled surface of the core, further refinement of our classification method requires a statistically significant number of cores with known validation. Thus, further refinement is reserved for future work.

4. Conclusions

This paper tested the validity of using photogrammetry and image processing techniques to detect layer divisions and aggregate gradation within asphalt cores with the aim of developing a non-destructive method for roadway sample analysis. The process explored in this research produced a distortion-free image of the cylindrical surface of the core elimination the need to slice the core as has been required in past work. From the distortion-free image, layers were detected using a simple algorithm which was sufficiently accurate to show the potential of this non-destructive method; however, further work on layer detection should focus on incorporating more parameters which will highlight layer interfaces even when core conditions are not ideal.

From the distortion-free image, an estimate of the gradation was also made of four cores with known aggregate gradations. For aggregates larger than 2 mm, the image processing method proposed performed well; however, the calculated gradations under-represented aggregates smaller than 2 mm. There are two probable causes for this under-representation which further research could explore. First, the density of the point cloud produced from the photogrammetric reconstruction might be able to be increased with a higher image count higher resolution camera. Second, in this work, the color of each pixel in the final surface image is determined by the color values which Metashape assigns to each point in the photogrammetric reconstruction. The method Metashape uses to assign the color to each reconstructed point is unknown. Future research could focus on calculating the color of each reconstructed point which preserves more of the resolution of the original core photographs.

Finally, future work on this topic should develop a more robust method of classifying the gradation curve. The point system used in this paper was used only as a proof of concept. To develop a robust classification system, more validations cores are needed.

In the end, this paper demonstrates that photogrammetric processes can be used to create 2D images of the curved surface of a cylindrical core, and that these distortion-free images can be used to detect both layer divisions and aggregate gradation automatically and non-destructively.

Acknowledgments

Not Applicable

ORCID

Joshua Carpenter https://orcid.org/0000-0001-5192-8675
Jinha Jung https://orcid.org/0000-0003-1176-3540
Jusang Lee https://orcid.org/0000-0002-4527-1678

References

Bruno L, Parla G, Celauro C (2012) Image analysis for detecting aggregate gradation in asphalt mixture from planar images. *Construction and Building Materials* 28(1):21-30, DOI: 10.1016/j.conbuildmat.2011.08.007

Buchanan MS, Brown ER (1999) Development and potential use of an automated aggregate gradation device. *Transportation Research Record* 1673(1):81-88

Chen WF, Liew JYR (Eds.) (2002) The civil engineering handbook. CRC Press

du Plessis A, Boshoff WP (2019) A review of X-ray computed tomography of concrete and asphalt construction materials. *Construction and Building Materials* 199:637-651, DOI: 10.1016/j.conbuildmat.2018.12.049

Fadil H, Jelagin D, Partl MN (2022) Spherical indentation test for quasi-non-destructive characterization of asphalt concrete. *Materials and Structures* 55(3):102, DOI: 10.1617/s11527-022-01945-5

Farcas FA (2012) Evaluation of asphalt field cores with simple performance tester and X-ray computed tomography. KTH Royal Institute of Technology

INDOT (2021) Quantitative extraction of asphalt/Binder and gradation of extracted aggregate from HMA Mixtures. *Indiana Department of Transportation Division of Materials and Tests* ITM(571-21)

INDOT (2022) Section 401 - Quality control / quality assurance. Hot Mix Asphalt Pavement, Retrieved April 25, 2023, https://www.in.gov/dot/div/contracts/standards/book/sep21/400-2022.pdf

Kadium N sajad, Sarsam SI (2020) Evaluating asphalt concrete properties by the implementation of ultrasonic pulse velocity. *Journal of Engineering* 26(6):140-151, DOI: 10.31026/j.eng.2020.06.12

Kanan C, Cottrell GW (2012) Color-to-Grayscale: Does the method matter in image recognition? *PLoS ONE* 7(1):e29740, DOI: 10.1371/journal.pone.0029740

Levenberg E, Manevich A (2013) Determination of bulk volume of asphalt specimens with image-based modeling. *International Journal of Transportation Science and Technology* 2(1):1-13, DOI: 10.1260/2046-0430.2.1.1

Maiti A, Chakravarty D, Biswas K, Halder A (2017) Development of a mass model in estimating weight-wise particle size distribution using digital image processing. *International Journal of Mining Science and Technology* 27(3):435-443, DOI: 10.1016/j.ijmst.2017.03.015

Obaidat MT, Ghuzlan KA, Alawneh MM (2017) Analysis of volumetric properties of bituminous mixtures using cellular phones and image processing techniques. *Canadian Journal of Civil Engineering* 44(9):715-726, DOI: 10.1139/cjce-2017-0085

Shi L, Wang D, Jin C, Li B, Liang H (2020) Measurement of coarse aggregates movement characteristics within asphalt mixture using digital image processing methods. *Measurement* 163:107948, DOI: 10.1016/j.measurement.2020.107948

Tashman L, Wang L, Thyagarajan S (2007) Microstructure characterization for modeling HMA behaviour using imaging technology. *Road Materials and Pavement Design* 8(2):207-238, DOI: 10.1080/14680629.2007.9690073

Tielmann MRD, Hill TJ (2018) Air void analyses on asphalt specimens using plane section preparation and image analysis. *Journal of Materials in Civil Engineering* 30(8):04018189, DOI: 10.1061/(ASCE)MT.1943-5533.0002422

Vadood M, Johari MS, Rahaei AR (2014) Introducing a simple method to determine aggregate gradation of hot mix asphalt using image processing. *International Journal of Pavement Engineering* 15(2):142-150, DOI: 10.1080/10298436.2013.786076

Xing C, Xu H, Tan Y, Liu X, Ye Q (2019) Mesostructured property of aggregate disruption in asphalt mixture based on digital image processing method. *Construction and Building Materials* 200:781-789, DOI: 10.1016/j.conbuildmat.2018.12.133

Yue ZQ, Bekking W, Morin I (1995) Application of digital image processing to quantitative study of asphalt concrete microstructure. *Transportation Research Record* 1492:53-60

Zargar M, Bullen F (2021) Non-destructive assessment of the quality of asphalt laboratory samples. *IOP Conference Series: Materials Science and Engineering* 1075(1):012023, DOI: 10.1088/1757-899X/1075/1/012023

Zelelew HM, Papagiannakis AT (2011) A volumetrics thresholding algorithm for processing asphalt concrete X-ray CT images. *International Journal of Pavement Engineering* 12(6):543-551, DOI: 10.1080/10298436.2011.561345